

### ASME Journal of Applied Mechanics Online journal at:

https://asmedigitalcollection.asme.org/appliedmechanics



# **Dezhong Tong**

Department of Mechanical and Aerospace Engineering, University of California, Los Angeles, CA 90095 e-mail: ttll960308@g.ucla.edu

## Md Ibrahim Khalil

Department of Mechanical Engineering, University of Maine, Orono, ME 04473 e-mail: md.khalil@maine.edu

# **Matthew Justin Silva**

Department of Mechanical and Aerospace Engineering, University of California, Los Angeles, CA 90095 e-mail: mattsilva2@g.ucla.edu

# **Guanjin Wang**

Department of Mechanical and Aerospace Engineering, University of California, Los Angeles, CA 90095 e-mail: gjwang@g.ucla.edu

# Bashir Khoda<sup>1</sup>

Associate Professor Department of Mechanical Engineering, University of Maine, Orono, ME 04473 e-mail: bashir.khoda@maine.edu

# Mohammad Khalid Jawed<sup>1</sup>

Associate Professor
Department of Mechanical and Aerospace
Engineering,
University of California,
Los Angeles, CA 90095
e-mail: khalidjm@seas.ucla.edu

# Mechanical Response of Fisherman's Knots During Tightening

The fisherman's knot, renowned for its strength and reliability, finds applications in engineering and medicine. However, a comprehensive understanding of its mechanics remains limited in scientific literature. In this paper, we present a systematic study of the tightening behavior of the fisherman's knot through a combined approach of tabletop experiments and discrete elastic rods simulations. Our experimental setup involves gradually applying tension to the two ends of the fisherman's knot until it fractures. We observed a correlation between the knot's material properties and its behavior during tightening, leading up to fracture. The tightening process of the fisherman's knot exhibits distinct "sliding" or "stretching" motions, influenced by factors such as friction and elastic stiffness. Furthermore, the failure modes of the knot (material fracture and topological failure) are determined by an interplay between elastic stiffness, friction, and initial conditions. This study sheds light on the underlying mechanics of the fisherman's knot and provides insight into its behavior during the tightening process, contributing to the broader understanding of the mechanics of knots in practical applications.

[DOI: 10.1115/1.4063895]

Keywords: computational mechanics, elasticity, mechanical properties of materials, knots

### 1 Introduction

Mathematically, a knot is represented by a closed curve in threedimensional space that forms a tangled loop or knotted string, which cannot be untangled without cutting it [1]. However, the study of knots has expanded beyond mathematics and found applications in diverse scientific disciplines. The combination of topology and material properties gives rise to a wide range of mechanical

<sup>1</sup>Corresponding authors.

Contributed by the Applied Mechanics Division of ASME for publication in the JOURNAL OF APPLIED MECHANICS. Manuscript received September 20, 2023; final manuscript received October 21, 2023; published online November 16, 2023. Tech. Editor: Pradeep Sharma.

characteristics exhibited by different knots in various contexts. In the domain of navigation, it is common knowledge among fishermen and sailors that tying a knot in a rope severely reduces its tensile strength [2]. Material scientists observed that knots are almost always present in sufficiently long polymers [3]. In biology, knots can be found in DNA molecules and protein structures [4]. They serve various purposes, such as blocking DNA replication and gene transcription [5], increasing antibiotic sensitivity [6], and catalyzing enzymatic reactions [7,8]. In the field of engineering, the buckling of knots [9] and their tangled configurations [10] have increasingly attracted researchers' interest. Investigating the tangling and untangling of knots sheds light on the energy storage and release mechanisms governed by topological constraints [11,12]. However, given the large number of physical

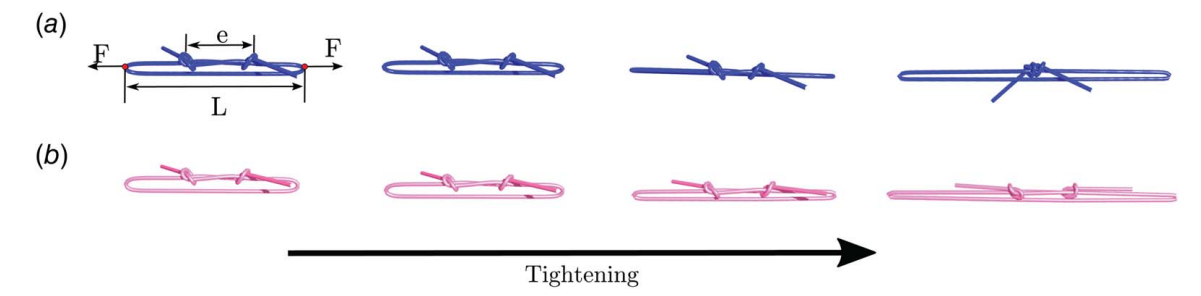


Fig. 1 Simulation snapshots illustrating the knot-tightening process. Axial load *F* on two nodes (marked by circles) at a distance *L* tightens the knots: (a) sliding motion where the knotted distance e gradually decreases to zero during tightening and (b) stretching motion where e slowly increases during tightening.

parameters (material, topological, friction) and geometric nonlinearity involved, the mechanical response of several common types of knots (e.g., fisherman's knot) remains unexplored.

One main direction of knot research is to explore the influence of material, frictional, and geometric properties on the mechanical performance of knots. In prior works, researchers have typically employed theoretical analysis, simulations, and experiments either separately or in combination to study knots. One exciting research direction is optimization problems related to the topology of knots. Moulton et al. [13] studied a stable knot configuration of an elastic rod or strip clamped in a specific geometry without self-contact. A theoretical analysis was developed to demonstrate that such geometry exists only within a certain range of material properties. Another interesting problem is exploring the nonlinear geometric behavior of knots. Clauvelin et al. [14] derived an analytical expression for the equilibrium of a thin knotted elastic rod subject to pulling force and twisting moment applied at two ends. They showed instability in overhand knots when the twisting moments on the two ends reached specific thresholds. In Ref. [9], it was demonstrated that instability of an overhand knot could occur without any twisting moment when the rod radius is relatively thick. When the unknotting number of an overhand knot exceeds one, instability can always occur simply by pulling the two tails of the knot. Ibrahim Khalil et al. [15] investigated the mechanical behavior of overhand knots by manipulating the friction force on an elastic rod. The objective was to understand the mechanics of overhand knots at various unknotting numbers through a systematic variation of friction. The findings revealed that multiple forces and moments come into play during rod-rod contact, which is significant in any experimental setup that unravels the fundamental aspects of overhand knot mechanics.

In addition to the studies mentioned above, the strength and fracture of knots are always critical in engineering and medicine. Several recent studies have focused on the mechanical performance of various knots. Sano et al. [16] investigated the mechanical performance of a clove hitch's knot when tied around a rigid cylinder. By implementing finite element simulations [17] and experimental studies, their study pointed out that the tension of the knot in the contact region with the rigid body will decay to zero when the region is away from the loading end. Reference [18] studied the influence of material flexibility on knot tying. When tying a knot with a rod, the flexibility of the rod affects the untangling of the knot, which can be considered a form of failure. The study concluded that the increased flexibility of a rod is advantageous for tying various knots. A number of studies focused on the unique mechanical responses of knots with specific geometries. In Ref. [19], the influence of knot configurations on the tensile characteristics was studied for various surgeon knot configurations in oral and maxillofacial surgery operations. Calvaresi et al. [20] combined force spectroscopy with quantum chemical calculations to report the force response of small-molecule trefoil knots during tigthening. In Ref. [21], theoretical expressions are derived for the tightening and untightening forces of a trefoil and cinquefoil overhand knots. The effects of geometrical and material parameters on such knots are captured by the theoretical framework. Further, Jawed et al. [22] expanded the framework of Ref. [21] to consider the case of overhand knots dominated by friction.

In this paper, we focus on the mechanical properties of a fisherman's knot. Fisherman's knot is a type of fundamental knot that is prevalent in fishing. Recently, researchers in medicine found that tying a fisherman's knot is a simple, efficacious, and safe suturing technique for immediate hemostasis and damage repair after operations [23]. Although the fisherman knot is known for its strength and reliability in many fields, few prior works studied its mechanical properties systematically. In this paper, we report experiments to show that the tightening of a fisherman's knot can be divided into three modes: stretching, sliding, and untangling. This is further substantiated by numerical simulations based on the discrete elastic rods (DER) algorithm. We quantitatively demonstrate the influence of material parameters on the tightening and failure of the fisherman's knot. As shown in Fig. 1, we observed two tightening modes, including "sliding" and "stretching" in experiments and simulations. Correspondingly, there are three failure modes: (1) "sliding" then fracture, (2) "stretching" then fracture, and (3) "untangling," which are discussed in detail in this study. A scaling analysis is employed to extract the primary influential physical factors from the geometrical and material properties of this system, which govern the mechanics of the fisherman's knots.

The paper is organized as follows. The topology of fisherman's knots and the statement of the problem are presented in Sec. 2. Then, we formulate the numerical framework, which couples the DER-based rod model and frictional contact, to study the tightening process of a fisherman's knot in Sec. 3.1. Next, we discuss our experimental protocol in Sec. 4, including the material preparation and experimental setup. All experimental and simulation results are discussed in Sec. 5. Finally, we provide concluding remarks and discuss possible future research avenues in Sec. 6.

### 2 Problem Statement

A fisherman knot is a symmetrical assembly of two trefoil overhand knots, as shown in Fig. 1(a). Further details on tying the knot will be provided later in the manuscript (Fig. 4). Generally, a fisherman's knot can be treated as a slip knot. In other words, if applying forces on the two ends, the two knotted regions can slide along the closed loop. As the tightening force **F** on the two ends increases, the knotted distance e will decrease since two knotted regions are supposed to slide. However, we observed that the fisherman's knot can be a "dead" knot when the material properties or the boundary condition changes, as shown in Fig. 1(b). In this problem, the potential contributing properties are the rod's axial stretching stiffness  $k_s$ , bending stiffness  $k_b$ , twisting stiffness  $k_t$ , friction coefficient  $\mu$ , rod radius h, knotted distance e, and end-to-end distance L, which will be discussed in Sec. 4. The motivation for this work lies in exploring the application domain by studying the correlation between the geometric evolution of the fisherman's knot while being tightened and the mentioned parameters. This

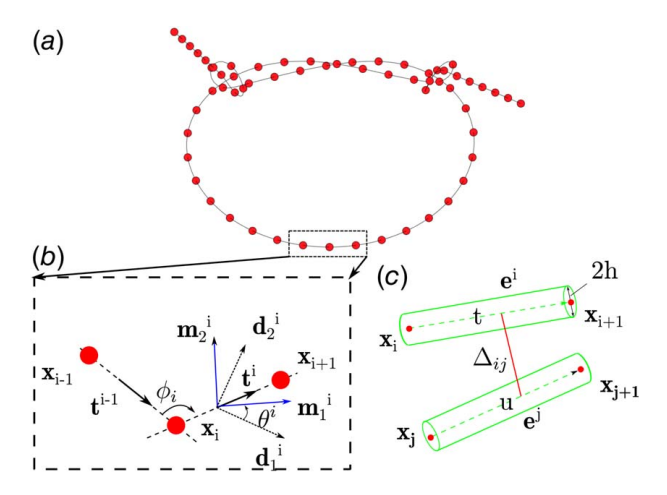


Fig. 2 Illustration of discrete schematics and relevant notations: (a) discrete schematic of an elastic rod, (b) discrete notations for the reference frame  $[\mathbf{d}_1^i, \mathbf{d}_2^i, \mathbf{t}']$ , the material frame  $[\mathbf{m}_1^i, \mathbf{m}_2^i, \mathbf{t}']$ , the twist angle  $\theta^i$ , and the turning angle  $\phi_i$ , and (c) schematic diagram of a contact pair showing the edges  $\mathbf{e}^i$ 

investigation aims to yield valuable insight into this knot's behavior, e.g., the load bearing capability, for practical use.

### 3 Numerical Framework

In this section, we present the approach to accurately simulate the tightening process of a fisherman's knot. We utilize the DER method [24,25] to capture the elastic energies associated with the nonlinear deformations in the knot. The physical accuracy of DER has been extensively validated in prior studies, including the coiling of rods on the ground [26], instability of the overhand knots [9], and the buckling of rods [27]. To account for rod-rod contact during the knot formation, we employ a penalty-energy-based contact framework [28,29]. This framework ensures the proper consideration of the interaction between rods in the simulation, thereby enhancing the accuracy and realism of the results. By combining the DER approach for capturing elastic deformations with the penalty-energy-based contact framework for handling rod-rod frictional contact, we achieve a comprehensive and robust simulation of the tightening process of a fisherman's knot.

**3.1 Discrete Elastic Rods.** The DER algorithm, developed by Bergou et al. [24], captures the dynamics of a Kirchhoff elastic rod, including geometric nonlinearity. In this section, we discuss the construction of the equations of motion (EOM) for a rod under frictional contact.

As illustrated in Fig. 2(a), the centerline of the elastic rod is discretized into N+1 nodes, denoted as  $[\mathbf{x}_0, ..., \mathbf{x}_N]$ , resulting in N edges  $[\mathbf{e}^0, ..., \mathbf{e}^{N-1}]$  such that  $\mathbf{e}^i = \mathbf{x}_{i+1} - \mathbf{x}_i$  and  $0 \le i < N$ . Hereafter in this section, all node-based quantities are denoted with subscripts (e.g.,  $\mathbf{x}_i$ ) and all edge-based quantities are denoted with superscripts (e.g.,  $e^i$ ). In this discrete model, each edge  $e^i$  possesses an orthogonal reference frame  $[\mathbf{d}_1^i, \mathbf{d}_2^i, \mathbf{t}^i]$  and an orthogonal material frame  $[\mathbf{m}_1^i, \mathbf{m}_2^i, \mathbf{t}^i]$ . The shared director,  $\mathbf{t}^i = \mathbf{e}^i / \|\mathbf{e}^i\|$  in these two frames, corresponds to the edge tangent between successive nodes. The reference frame  $[\mathbf{d}_1^i, \mathbf{d}_2^i, \mathbf{t}^i]$  is arbitrarily initialized at the initial time (t=0), and parallel transported in time from the tangent  $\mathbf{t}^i$ (t) at time t to the tangent  $\mathbf{t}^{i}$   $(t + \Delta t)$  at time  $t + \Delta t$ , where  $\Delta t$  represents the time-step size. In Fig. 2(b), the material frame at the *i*th edge is derived from the reference frame at the same edge by applying a rotation  $\theta^i$  about  $\mathbf{t}^i$  and material frames are used to evaluate the twist along the rod. Consequently, the rod's centerline can be represented by a total of 4N + 3 degrees-of-freedom (DOF), consisting of 3(N+1) degrees-of-freedom for nodal positions and N

degrees-of-freedom for twist angles of each edge. The degrees-of-freedom vector can be expressed as

$$\mathbf{q} = [\mathbf{x}_0, \theta^0, \mathbf{x}_1, \theta^1, \mathbf{x}_2, \theta^2, \dots, \mathbf{x}_{N-1}, \theta^{N-1}, \mathbf{x}_N]^T$$
 (1)

where T is the transpose operator.

The EOM can be constructed based on the elastic energies of the rod, including stretching, bending, and twisting energies, as well as external forces such as contact and friction. First, the stretching energy is defined as

$$E_s = \sum_{i=0}^{N} \frac{1}{2} k_s \left( 1 - \frac{\|\mathbf{e}^i\|}{\|\bar{\mathbf{e}}^i\|} \right)^2 \|\bar{\mathbf{e}}^i\|$$
 (2)

where  $k_s$  is the stretching stiffness and  $\bar{\mathbf{e}}^i$  represents the undeformed (stress-free) edge. Hereafter, the bar notation denotes quantities in undeformed state. For a rod made of linear elastic material,  $k_s = EA$ , where E is Young's modulus and A is the cross-sectional area.  $\bar{\mathbf{e}}^i$ , represents the undeformed edge.

Next, the bending energy is given by

$$E_b = \sum_{i=1}^{N} \frac{k_b}{\|\bar{\mathbf{e}}^i\| + \|\bar{\mathbf{e}}^{i-1}\|} (\boldsymbol{\kappa} - \bar{\boldsymbol{\kappa}})^T (\boldsymbol{\kappa} - \bar{\boldsymbol{\kappa}})$$
(3)

where  $k_b$  is the bending stiffness. When the material is under the linear elastic assumption,  $k_b = EI$ , where  $I = \frac{\pi h^4}{4}$  is the moment of inertia, and h is the rod radius. In Eq. (3),  $\kappa$  and  $\bar{\kappa}$  are deformed and natural curvature vectors, respectively. Here,  $\|\kappa\| = 2\tan{(\phi_i/2)}$ , where  $\phi_i$  is the turning angle, as illustrated in Fig. 2(b).

Additionally, the twisting energy is defined as

$$E_t = \sum_{i=1}^{N} \frac{1}{2} \frac{k_t}{\|\bar{\mathbf{e}}^i\|} (\tau_i - \bar{\tau}_i)^2$$
 (4)

where  $k_t$  is the twisting stiffness. For a linear elastic material,  $k_t = GJ$ , where  $G = \frac{E}{2(1 + \nu)}$  is the shear modulus,  $\nu$  is the Poisson's

ratio, and  $J = \frac{\pi r_0^4}{2}$  is the polar second moment of inertia. In Eq. (4),  $\tau_i = \theta^{i+1} - \theta^i + \Delta \tau^{\rm ref}$  represents the discrete twist at node  $\mathbf{x}_i$ , and  $\Delta \tau^{\rm ref}$  is the discrete reference twist.

Now, the internal force at the *i*th DOF,  $\mathbf{F}_{i}^{int}$ , can be defined in terms of energy as

$$\mathbf{F}_{i}^{\text{int}} = \frac{\partial (E_s + E_b + E_t)}{\partial \mathbf{q}}.$$
 (5)

where  $\mathbf{q}_i$  represents the *i*th element in the DOF vector. Then, the EOM for the system can then be written as

$$\mathbf{M}\ddot{\mathbf{q}} - \mathbf{F}^{\text{int}} - \mathbf{F}^{\text{ext}} = 0 \tag{6}$$

where  $\mathbb M$  is the mass matrix,  $\ddot{q}$  is the acceleration vector,  $F^{\text{ext}}$  represents the external forces, and  $F^{\text{int}}$  is the internal force vector.

In the DER algorithm, the implicit Euler method is employed for time integration of the EOM, updating the status of  $\mathbf{q}$  from time  $t_{\rm old}$  to  $t_{\rm new} = t_{\rm old} + \Delta t$ . The EOM is formulated as

$$f(\mathbf{q}_{\text{new}}) \equiv \frac{\mathbb{M}}{\Delta t} \left( \frac{\mathbf{q}_{\text{new}} - \mathbf{q}_{\text{old}}}{\Delta t} - \dot{\mathbf{q}}_{\text{old}} \right) - \mathbf{F}_{\text{new}}^{\text{int}} - \mathbf{F}_{\text{new}}^{\text{ext}} = 0$$
 (7)

where the elastic force vector  $\mathbf{F}_{\text{new}}^{\text{int}}$  is

$$\mathbf{F}_{\text{new}}^{\text{int}} = -\frac{\partial (E_s + E_b + E_t)_{\text{new}}}{\partial \mathbf{q}_{\text{new}}}$$
(8)

 $\mathbf{q}_{\text{new}} = \mathbf{q}(t_{\text{new}})$  is unknown,  $\mathbf{q}_{\text{old}} = \mathbf{q}(t_{\text{old}})$  is known,  $\dot{\mathbf{q}}_{\text{old}}$  is the velocity vector at  $t_{\text{old}}$ ,  $\mathbf{F}_{\text{new}}^{\text{ext}}$  is the external force vector  $t_{\text{new}}$ , and  $\mathbb{M}$  represents the diagonal mass matrix with a size of  $(4N+3)\times(4N+3)$ . The

Table 1 Material properties of rods in the experiments

Material properties	Nylon	Polypropylene	Pink VPS	Green VPS
Stretching stiffness (Pa·m²) Bending stiffness (Pa·m⁴) Friction coefficient (measured)	$7.34 \times 10^{4}  4.31 \times 10^{-5}  0.46 \pm 0.02$	$3.90 \times 10^4$ $1.18 \times 10^{-4}$ $0.63 \pm 0.01$	$   \begin{array}{l}     1.70 \\     4.34 \times 10^{-6} \\     0.54 \pm 0.01   \end{array} $	$ 22.15 5.67 \times 10^{-5} 0.37 \pm 0.01 $

notation () indicates the derivative with respect to time. In our studied case,  $\mathbf{F}^{\text{ext}}$  includes the contact forces  $\mathbf{F}^{c}$  and the friction forces  $\mathbf{F}^{r}$ . The Newton–Raphson method is employed to find the root of  $f(\mathbf{q}_{\text{new}}) = 0$  in Eq. (7), where the Jacobian of Eq. (7) is defined as follows:

$$\mathbf{J}ij = \frac{m_i}{\Delta t^2} \delta ij + \frac{\partial^2 (E_s + E_b + E_t)}{\partial \mathbf{q}i \partial \mathbf{q}j} - \mathbf{J}_{ij}^c - \mathbf{J}_{ij}^r$$
(9)

where  $m_i$  is the *i*th diagonal element in mass matrix  $\mathbb{M}$ ,  $\delta_{ij}$  denotes the Kronecker delta, and  $\mathbf{J}^c_{ij}$  and  $\mathbf{J}^r_{ij}$  represent the Jacobians of the contact forces and the friction forces, respectively. The subscript ij indicates the *i*th row and *j*th column of the Jacobian.

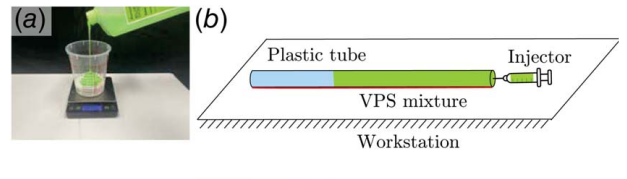




Fig. 3 Manufacturing steps of VPS rods: (a) preparation of VPS mixture, (b) schematic of the manufacturing process, and (c) samples of fabricated rods

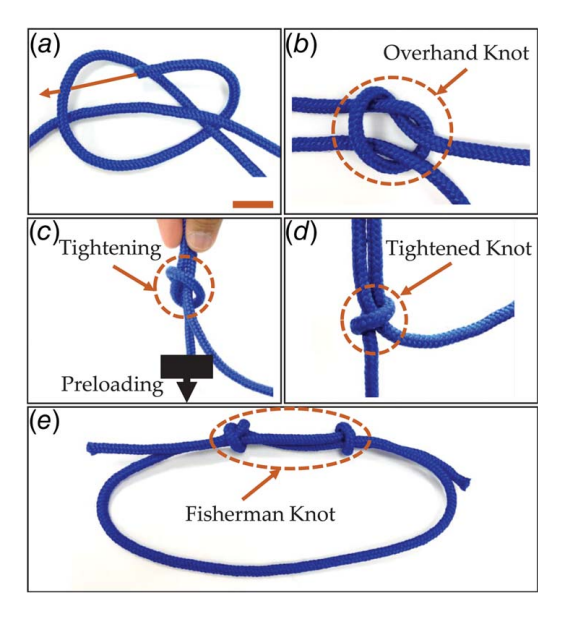


Fig. 4 Steps of knot preparation: (a) tying an overhand knot around one tail to form a knotted region, (b) visualization of the topology of the loosely knotted region in a fisherman's knot, (c) tightening the knotted region with pre-loading, (d) visualization of the topology of the tightened knotted region in a fisherman's knot, and (e) the prepared fisherman's knot. Scale bar is 2 cm

**3.2 Penalty-Energy-Based Contact.** In our numerical framework, friction is implemented using Coulomb's friction model. References [28,29] presented a penalty-based energy approach for introducing frictional contact responses as constraints, accurately capturing Coulomb's friction. In this section, we formulate the penalty energies and discuss the computation of frictional responses based on these energies.

In our framework, a contact pair is formed by combining two edges,  $\mathbf{e}^i$  and  $\mathbf{e}^j$ , as depicted in Fig. 2(c). This contact pair consists of nodes  $\mathbf{x}_i$ ,  $\mathbf{x}_{i+1}$ ,  $\mathbf{x}_j$ , and  $\mathbf{x}_{j+1}$ . Thus, we can represent a contact pair as the vector concatenation  $\mathbf{x}_{ij} := (\mathbf{x}_i, \mathbf{x}_{i+1}, \mathbf{x}_j, \mathbf{x}_{j+1})$  (size  $12 \times 1$ ). Based on off Lumelsky algorithm [30], the minimal distance between two edges can be computed as  $\Delta_{ij} = \|(1-t)\mathbf{x}_i + t\mathbf{x}_{i+1} - (1-u)\mathbf{x}_j - u\mathbf{x}_{j+1})\|$ , where t and u are differentiable quantities expressing the position of the contact point in the contact pair. The contact energy formulation  $E^c$ , based on Refs. [28,29], is given by

$$E^{c}(\Delta, \delta)$$

$$= \begin{cases} (2h - \Delta)^{2} & \Delta \in (0, 2h - \delta] \\ \left(\frac{1}{K_{1}}\log\left(1 + \exp\left(K_{1}(2h - \Delta)\right)\right)\right)^{2} & \Delta \in (2h - \delta, 2h + \delta) \\ 0 & \Delta \geq 2h + \delta \end{cases}$$
(10)

where  $\delta$  is a hyperparameter called distance tolerance, which controls the magnitude of the penetration, h is the rod radius, and  $K_1 = 15/\delta$  indicates the stiffness of the energy curve. The piecewise contact energy, as shown in Eq. (10), is continuous and differential in the force region so that we can compute the required normal contact force with chain rule based on that with

$$\mathbf{F}^{c} = \frac{\partial E^{c}}{\partial \Delta} \frac{\partial \Delta}{\partial \mathbf{q}} \tag{11}$$

Then, we calculate the friction forces based on Coulomb's friction law, which states that the magnitude of frictional force  $\|\mathbf{F}^f\|$  satisfies the following conditions: (1) it is equal to  $\mu \|\mathbf{F}^c\|$  during sliding, (2) it lies in the range  $[0, \mu \|\mathbf{F}^c\|]$  when sticking, and (3) it is independent of the magnitude of velocity.

Here  $\mu$  represents the friction coefficient, and  $\|\mathbf{F}^c\|$  denotes the magnitude of the normal force acting on the body. To smoothly transition from sticking friction to sliding friction, we propose a formulation for frictional responses

$$\mathbf{F}^{f} = -\gamma \mu \| \mathbf{F}^{c} \| \hat{\mathbf{v}}^{Trel}$$

$$\gamma(\| \mathbf{v}^{Trel} \|, v_{s}) = \frac{2}{1 + \exp(-K_{2} \| \mathbf{v}^{Trel} \|)} - 1$$
(12)

In Eq. (12),  $v_s$  (m/s) represents the desired slipping tolerance, and the stiffness parameter  $K_2(v_s) = 15/v_s$  controls the system's behavior.  $\mathbf{v}^{\text{Trel}}$  represents the relative tangential velocity between the two contacting bodies. We introduce an artificial quantity,  $\gamma$ , to control the transition from sticking to sliding. The value of  $\gamma$  depends on the magnitude of  $\mathbf{v}^{\text{Trel}}$ . When the relative tangential velocity is smaller than  $v_s$ ,  $\gamma$  scales the sliding friction forces to keep them within the range of sticking friction forces. When the relative tangential velocity is significant (larger than  $v_s$ ),  $\gamma$  approaches 1, ensuring a constant ratio (the ratio is  $\mu$ ) between the sliding friction force and the normal contact forces.

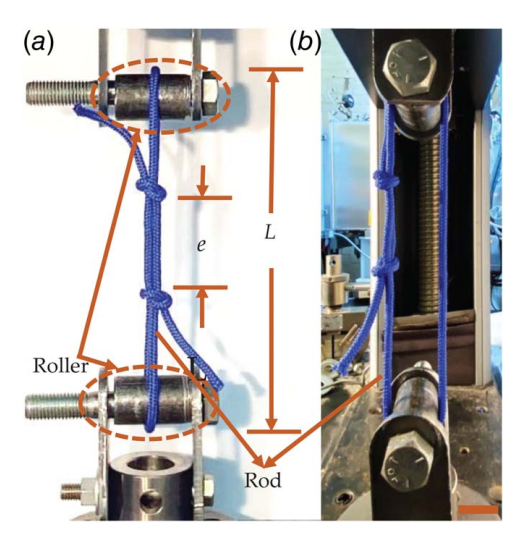


Fig. 5 Experimental setup for tightening a fisherman's knot using Instron: (a) front view and (b) side view. The knotted distance is denoted by e, and the end-to-end distance of the knot is denoted by L. Scale bar is 3 cm.

It is worth mentioning that both  $\mathbf{F}^c$  and  $\mathbf{F}^f$  are differentiable to the DOF vector, allowing us to compute the Jacobian of the frictional contact forces. By incorporating the computed frictional contact forces and Jacobians into Eqs. (7) and (9), we can solve for the nonlinear behavior of the fisherman knot and obtain measurements of the relative quantities in the simulation.

### 4 Experimental Study

This section includes the process of material preparation, knot preparation, and the experimental protocol. First, we discuss the preparation of materials required for the experiments. Next, we detail knot preparation and experimental protocol in the subsequent subsections.

**4.1 Material and Knot Preparation.** We used four different rod materials (polypropylene, nylon, vinyl polysiloxane (VPS)

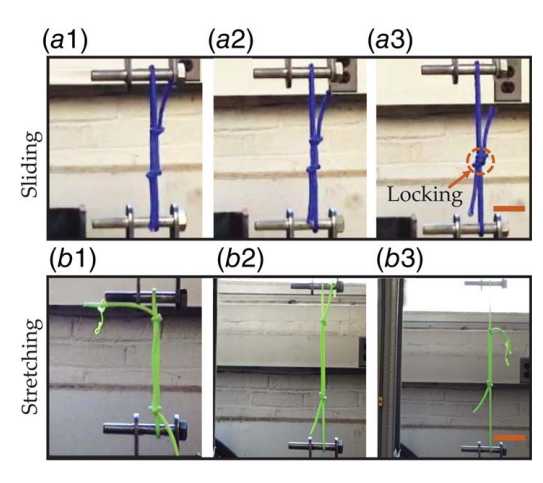


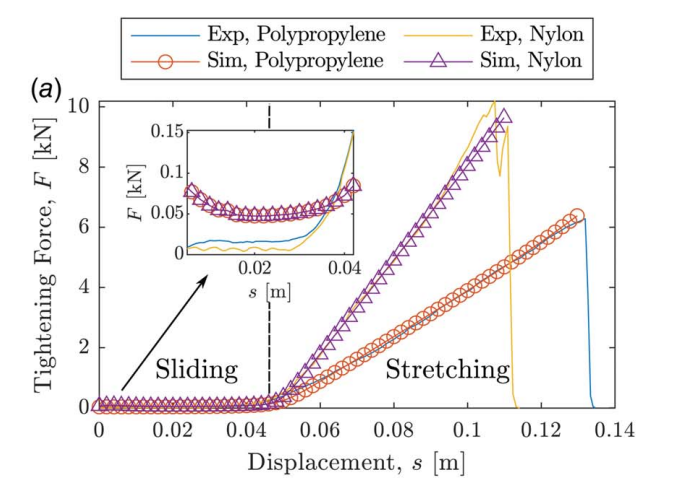
Fig. 6 Motion patterns during knot tightening and fracture: (a) sliding-stretching-fracture (experimental snapshots at (a1) t=0 s—initial configuration, (a2) t=10 s—two knotted regions keep sliding, and (a3) t=20 s—stretching occurs after two knotted regions meet and lock, continuing until fracture) and (b) stretching-fracture (experimental snapshots at (b1) t=0 s—initial configuration; (b2) t=10 s—the overall structure keeps stretching, (b3) t=20 s—stretching continues until fracture occurs). Scale bar is 5 cm for both (a) and (b).

rod with higher stiffness (green color), and lower stiffness (pink color)) to prepare the fisherman knot during the tensile experiments. The material properties of the different rods are stated in Table 1.

The diameter of all rods used in the investigation is 1/4 in. Polypropylene and Nylon rods are purchased from Gardzen, Rowland Heights, CA and West Coast Paracord, Fargo, ND, respectively, while the VPS rods are prepared in our laboratory. In this part, we discuss the manufacturing technique of VPS rods.

We used a mold-forming method to manufacture the VPS rods. First, we fixed a one-meter-long plastic tube onto a clean flat table as straight as possible. The tube will serve as the mold for manufacturing the VPS rods which are naturally straight. To manufacture "green" VPS rods, we mixed the catalyst and the base (Elite Double 32, Zhermack, Badia Polesine, Italy) at 1:1 mass ratio, as seen in Fig. 3(a). The mixture is placed in a compression chamber with 25 psi for a few minutes to expel any air bubbles. As shown in Fig. 3(b), it is then injected into a hollow PVC tube with inner radius of 1/4 in. The softer "pink" VPS rods are made following the same protocol but using a different catalyst and base (Elite Double 8, Zhermack).

The fisherman's knots used in our experiment involve the joining of two fishing lines or rods. To create a fisherman's knot, we initiate



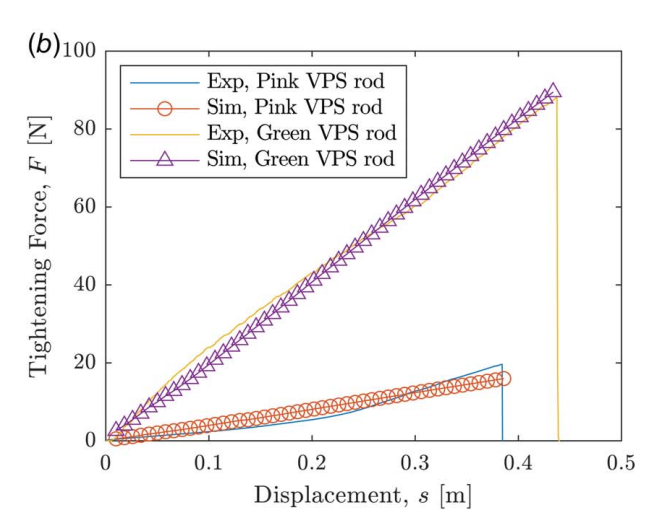


Fig. 7 Comparison of tightening force, F, (as a function of displacement, s) between numerical and experimental results for: (a) commercially available rods and (b) VPS rods. Note that the range of the y-axis is significantly different between the two plots. The vertical dashed line in (a) represents the transition from the sliding to the stretching region. For clarity, the inset in (a) shows F versus s relation only for the sliding region. The force, F, increases dramatically as the knot transitions from sliding to stretching.

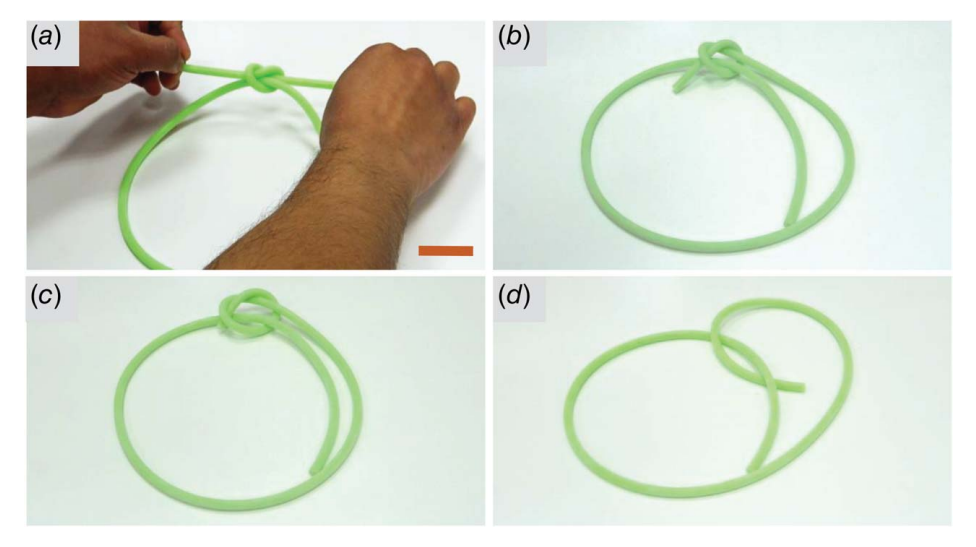


Fig. 8 Untangling of the fisherman's knot: (a) the VPS rod is tightened using hands and then released to move freely (t = 0 s), (b) position of the knot at t = 5 s, (c) loop shrinking continues to untangle the knot (t = 10 s), and (d) untangled knot (t = 15 s). Scale bar is 6 cm for all figures.

the process by crafting a basic overhand knot at one end of a rod. Subsequently, we thread the other rod through this overhand knot and proceed to tighten it. This exact procedure is replicated on the opposing end of the second rod. A visual representation of the step-by-step process is given in Fig. 4 using a polypropylene rod.

**4.2 Experimental Protocol.** To investigate the connection between material properties and knot performance, we devised a systematic tensile study using a universal testing machine (UTM). To minimize stress concentration at the gripper of the UTM, we opt for a single rod for knot preparation, which leads to the creation of a continuous loop as shown in Fig. 4. To conform with the same initial condition, a predefined loading is applied to uniformly tighten the fisherman's knots.

The process begins with crafting an overhand knot at one end of the rod, as illustrated in Fig. 4(a). The loose overhand knot's appearance is shown in Fig. 4(b). To tighten the overhand knot, we secure the knot with one hand while applying the pre-load denoted as  $F_p$ , to the free end of the knot. This tightening procedure is detailed in Fig. 4(c). We systematically vary the pre-load to achieve the desired tightness of the knot and subsequently assess

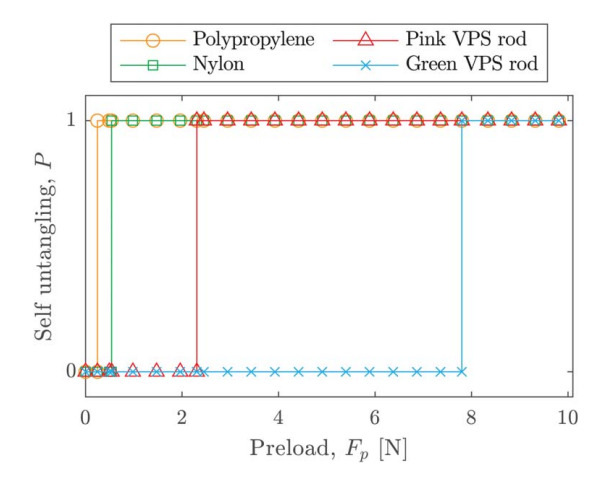


Fig. 9 Variation of self-untangling of the knot with pre-loading (tangled = 1, untangled = 0)

how this variation impacts the sliding force during the tensile tests. The appearance of the tightened overhand knot is captured in Fig. 4(d). This process is then replicated on the opposite end of the loop. The combination of the two properly tightened overhand knots results in the formation of the fisherman's knot, as illustrated in Fig. 4(e). The continuous loop setup is subsequently placed within the UTM machine supported by two rollers, serving as boundary conditions for tensile loading. The supporting roller has a diameter of 1.5 in., which is six times larger than the rod diameter and help alleviate the stress concentration during pulling. The tensile setup is depicted in Fig. 5. The spacing in the overhand knots, denoted as e, was consistently set at 15 cm and the end-to-end distance, L, was maintained at 25 cm in all trials. The experiment employed a 50 kN load cell and collected data at a frequency of 3 Hz. For the softer material (pink VPS), a 20 N load cell is utilized to collect the force-displacement data.

### 5 Results and Discussion

This section describes the mechanical behavior of the fisherman's knots during the tightening process. Due to the intricate interplay between material properties and topology, the knot undergoes one of three qualitatively distinct evolutions of topology: (1) the two overhand knotted region slides along the closed knot loop (Figs. 6(a1)-6(a3)), (2) the overall structure of the fisherman's knot stretches (Figs. 6(b1)-6(b3)), and (3) the knot untangles itself (Fig. 8). These three "motion patterns" are captured by both experiments and simulations. We first discuss the different motion patterns, and, then, describe the contributing physical factors.

**5.1 Motion Patterns.** The fisherman's knot is usually defined as a type of knot in which two overhand knotted regions can easily move along the closed knot loop. Referring to Fig. 6(a), this "sliding" motion pattern is observed in knots tied in polypropylene and nylon rods. Figures 6(a1)-6(a3) show snapshots from experiments and illustrate how the two knotted regions move towards each other during the sliding process. When the two knotted regions meet, the knot becomes "locked," and the entire structure is subjected to stretching until it eventually fractures. Figure 7(a) shows the relationship between the tightening force F and the displacement s from experiments and simulations. The parameter s represents the elongation of the end-to-end distance L. During the

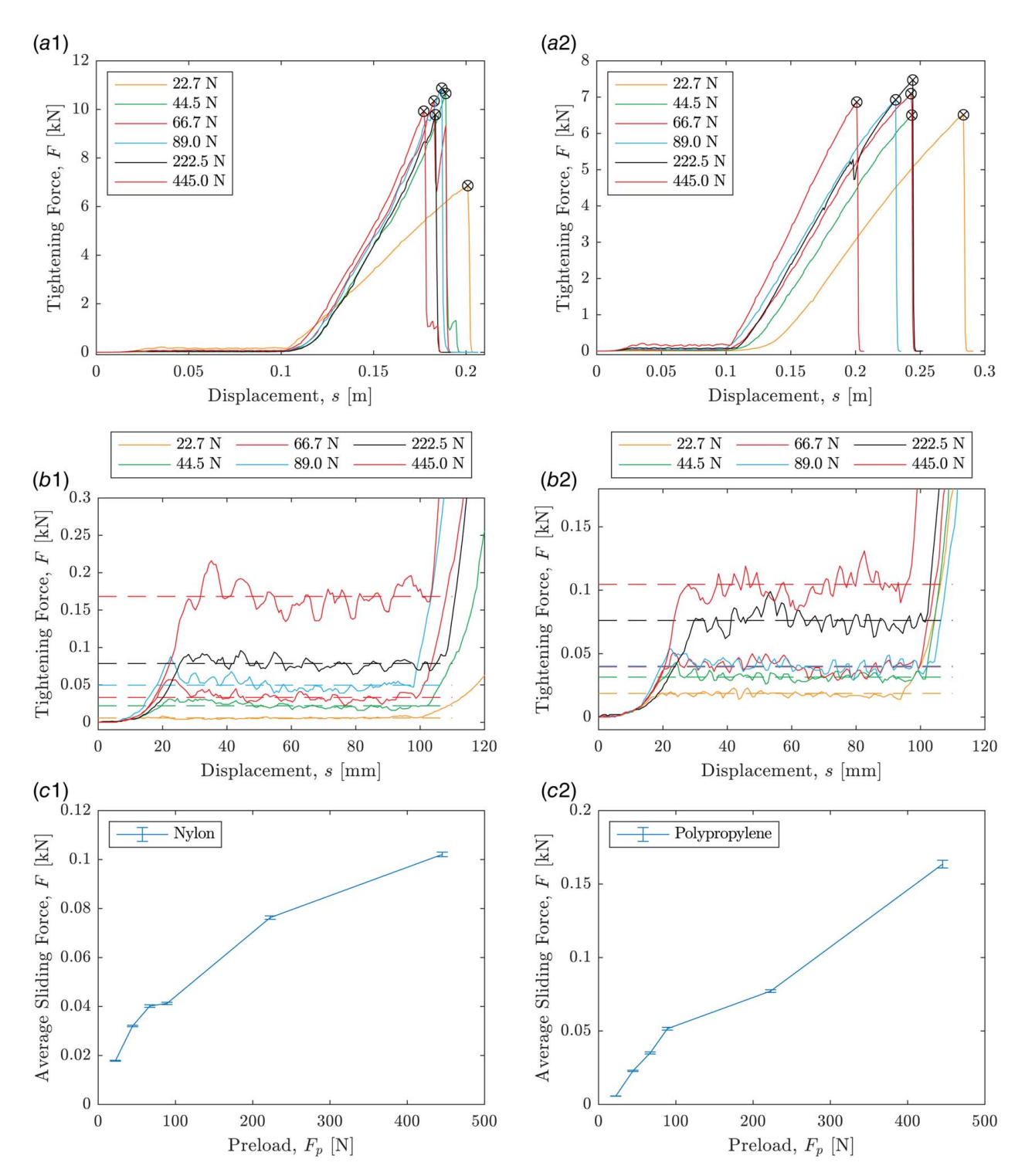


Fig. 10 Comparative analysis of tightening force variation with displacement at different pre-loadings: (a1) nylon rod and (a2) polypropylene. Zoomed-in view of the tightening force versus displacement relationship in the sliding region: (b1) nylon and (b2) polypropylene. Horizontal dashed lines represent the average tightening force. This average force monotonically increases with pre-load. Influence of pre-load  $F_p$  on average tightening force F in the sliding region: (c1) nylon and (c2) polypropylene.

sliding stage, the tightening force F remains stable and relatively low. However, when the knot is locked, the tightening force F increases significantly, following a slope that is directly proportional to the axial stretching stiffness  $k_s$ . This motion pattern of "sliding" allows for easy topology changes with minimal loading, while "stretching" makes the fisherman's knot more stable and resistant to changes in structure. In experiments, extreme stretching leads to material failure at  $s \approx 0.1$  m for Nylon and  $s \approx 0.13$  m for

Polypropylene. Note that material failure is not modeled in our simulations.

Notably, not all fisherman's knots follow the aforementioned sliding-stretching-fracture pattern. Experiments with Pink VPS and Green VPS rods, as shown in Fig. 6(b), revealed a second type of mechanical behavior where the two knotted regions seemingly "stick" to the closed knot loop and do not slide. In this case, the structure only stretches until it fractures during tightening.

Figure 7(b) shows the dependence of tightening force F on displacement s from experiments and simulations.

Additionally, the third—and, arguably, the simplest—pattern is "untangling" and is depicted in Fig. 8. It is well known that a knotted structure may or may not maintain its topology in the absence of external loads or boundary conditions [10]. In this scenario, the fisherman's knot untangles itself as soon as the boundary conditions imposed by human hands are removed. The frictional force acting on the rod may not be adequate to withstand the elastic forces arising from the knotted configuration. Our experimental observations on when a knot untangles itself are presented in the next section.

**5.2** Physical Ingredients. To identify the main contributing factors influencing the motion patterns of the fisherman's knot, we first list the physical ingredients of the system. The behavior of the fisherman's knots is governed by the coupling of geometry, loading process, and material properties. Geometric quantities include the rod radius h, knotted distance e, and end-to-end distance L. The material properties relevant to the process are bending stiffness  $k_b$ , stretching stiffness  $k_s$ , twisting stiffness  $k_t$ , rod density  $\rho$ , and friction coefficient  $\mu$ . For a homogeneous rod with a circular cross section that is made of linear elastic material, the expressions for  $k_s$ ,  $k_b$ , and  $k_t$  are available in Sec. 3.1. Commercially available ropes are often made of fibers or strands that are braided together. The elastic stiffness parameters  $(k_s, k_b, \text{ and } k_t)$  should be directly measured in that case. To ignore any effects of inertia, we kept the loading speed at 3.3 mm/s in our experiment, which is slow enough for the process to be quasi-static.

The last parameter, which eventually turned out to be a critical one, is the pre-loading force  $F_p$  (also see Fig. 4(c)). We hypothesized from our intuition, as well as experience of tying shoelace knots, that the amount of force used to tighten the two constituent overhand knots prior to completing the fisherman's knot influences the mechanical behavior. To test this hypothesis and assess the knot's stability as a function of pre-load, we tied a series of knots in four different materials and observed whether the knot untangles by itself. Figure 9 shows our experimental data on whether the knot untangles in the absence of boundary conditions (P = 0 in the plot) or maintains its knotted configuration (P=1). Depending on the material of the rod, there is a critical pre-load  $F_p$  that is needed for the knot to remain knotted without any external forces or boundary conditions. Our empirical observation is that pre-load can cause deformation of the cross section (i.e., circular cross section no longer remains circular) and affect the contact mechanics of the knotted region. However, our simulation employs a onedimensional rod model and does not model the structure as a 3D solid. Furthermore, the simulation uses the Coulomb friction model, which is a simplification of the contact mechanics involved here. Physically accurate simulation of the fisherman's knot that also captures the dependence on pre-load is left as a challenge to the computational mechanics community.

In the numerical simulations, we used the parameters from Table 1 to study the tightening process of the fisherman's knot. Note that we used a fitted friction coefficient, which is 1.0 for two VPS rods, for capturing the stretching motion pattern. Through numerical simulations and simple scaling analysis of energies, we find that gravity is negligible and changes in twisting stiffness have minimal influence on the motion patterns. Consequently, we disregard the impact of twisting stiffness  $k_t$  and rod density  $\rho$ . Furthermore, we find that the end-to-end distance L does not play a significant role in any motion pattern. Thus, we also exclude the end-to-end distance L from our analysis. The critical parameters of the system are now reduced to the knotted distance e, rod radius h, bending stiffness  $k_b$ , stretching stiffness  $k_s$ , friction coefficient  $\mu$ , and pre-load  $F_p$ . Dimensional analysis can be employed to extract dimensionless contributing parameters to facilitate a comprehensive understanding. Four dimensionless groups are obtained for this system: the friction coefficient  $\mu$ , the normalized stretching stiffness  $\bar{k}_s = k_s h^2/k_b$ , the normalized knot distance  $\bar{e} = e/h$ , and the normalized pre-loading force  $\bar{F}_p = F_p h^2/k_b$ .

5.3 Experiments to Explore the Role of Physical **Ingredients.** In both numerical and experimental studies, the knotted distance e (see Fig. 5) was used to evaluate the type of motion patterns exhibited by the fisherman's knot: when knotted distance e increases during the tightening process, we characterize the behavior of the knot as "stretching"; when e decreases or keeps constant during tightening, we characterize it as "sliding." Among the rods used in this study, only Nylon and Polypropylene showed both sliding and stretching behaviors. We used these two rods to perform a series of control experiments and systematically investigate the influence of pre-load  $F_p$ . Figures 10(a1) and 10(a2)show the tightening force as a function of imposed displacement s for the two rods at different values of pre-load. Keep in mind that knotted distance e monotonically increases (during stretching) or remains largely constant (during sliding) with displacement s. Force versus displacement data just for the sliding region is shown in Figs. 10(b1) and 10(b2). The force remains almost constant as a function of displacement during sliding. This is expected since the tightening force is directly related to the dynamic frictional force in the knotted region. The average tightening force is represented by the horizontal dashed lines in Figs. 10(b1) and 10(b2). As shown in Figs. 10(c1) and 10(c2), this average force monotonically increases with pre-load. Overall, these experiments reveal that pre-load can alter the relationship between the tightening force F and the displacement s, particularly in the sliding region. Increasing pre-load  $F_p$  led to higher tightening forces, indicating that pre-load can significantly impact the frictional contact responses in the knotted region. In the absence of a high-fidelity friction model that goes beyond Coulomb friction and a simulator that accounts for the deformation of the rod cross section, our numerical simulation cannot reproduce the dependence on pre-load. A direction for further work could be to accurately model this influence using a refined friction model that is, perhaps, developed using experimental data.

Due to limitations with the materials of the rods we used, it was not feasible to vary the friction coefficient  $\mu$  and the normalized stretching stiffness  $\bar{k}_s$ . In the future, a systematic investigation of the mechanical behavior of fisherman's knots as a function of all the physical ingredients is worth exploring.

### 6 Concluding Remarks

This paper presents a comprehensive experimental study investigating the mechanical properties of fisherman's knots. Our findings reveal three distinct motion patterns arising from the combined effects of the rod's geometrical and material properties. Additionally, we emphasize the significance of the knot-tying technique (pre-load in particular) in determining the resulting motion pattern. Through a qualitative analysis incorporating numeric simulations and experiments, this study fills a gap in our understanding of fisherman's knots. We also outlined room for development in numerical simulations. A simple friction model based on Coulomb friction was not able to faithfully reproduce some of the experimental observations. Moving forward, a more accurate friction model could be developed to computationally study fisherman's knots and various other commonly used knots where pre-loading affects the mechanical response.

## Acknowledgment

This research was funded by the National Science Foundation (Award # CMMI-2101751 and CMMI-2101745). M.K.J. and D.T. also acknowledge support from the National Science Foundation (Award # IIS-1925360).

A video outlining the steps to tie a fisherman's knot is available online.<sup>2</sup>

### Conflict of Interest

There are no conflicts of interest.

### **Data Availability Statement**

The datasets generated and supporting the findings of this article are obtainable from the corresponding author upon reasonable request.

### References

- [1] Lickorish, W. R., 2012, An Introduction to Knot Theory, Vol. 175, Springer Science & Business Media, New York.
- [2] Stasiak, A., Dobay, A., Dubochet, J., and Dietler, G., 1999, "Knotted Fishing Line, Covalent Bonds, and Breaking Points," Science, 286(5437), pp. 11–11.
- [3] Sumners, D., and Whittington, S., 1988, "Knots in Self-Avoiding Walks," J. Phys. A: Math. Gen., 21(7), p. 1689.
- [4] Marenduzzo, D., Micheletti, C., Orlandini, E., and Sumners, D. W., 2013, "Topological Friction Strongly Affects Viral Dna Ejection," Proc. Natl. Acad. Sci. U. S. A., 110(50), pp. 20081–20086.
- [5] Olavarrieta, L., Hernandez, P., Krimer, D. B., and Schvartzman, J. B., 2002, "Dna Knotting Caused by Head-On Collision of Transcription and Replication," J. Mol. Biol., 322(1), pp. 1–6.
- [6] Mann, J. K., 2007, DNA Knotting: Occurrences, Consequences & Resolution, The Florida State University, Tallahassee, FL.
- [7] Wagner, J. R., Brunzelle, J. S., Forest, K. T., and Vierstra, R. D., 2005, "A Light-Sensing Knot Revealed by the Structure of the Chromophore-Binding Domain of Phytochrome," Nature, 438(7066), pp. 325–331.
- [8] Lim, N. C., and Jackson, S. E., 2015, "Molecular Knots in Biology and Chemistry," J. Phys.: Condens. Matter, 27(35), p. 354101.
- [9] Tong, D., Choi, A., Joo, J., Borum, A., and Khalid Jawed, M., 2023, "Snap Buckling in Overhand Knots," ASME J. Appl. Mech., 90(4), p. 041008.
- [10] Patil, V. P., Sandt, J. D., Kolle, M., and Dunkel, J., 2020, "Topological Mechanics of Knots and Tangles," Science, 367(6473), pp. 71–75.
- of Knots and Tangles," Science, 367(6473), pp. 71–75.

  [11] Patil, V. P., Kos, Ž., Ravnik, M., and Dunkel, J., 2020, "Discharging Dynamics of Topological Batteries." Phys. Rev. Res., 2(4), p. 043196.
- Topological Batteries," Phys. Rev. Res., 2(4), p. 043196.
  [12] Patil, V. P., Tuazon, H., Kaufman, E., Chakrabortty, T., Qin, D., Dunkel, J., and Bhamla, M. S., 2023, "Ultrafast Reversible Self-Assembly of Living Tangled Matter," Science, 380(6643), pp. 392–398.

- [13] Moulton, D. E., Grandgeorge, P., and Neukirch, S., 2018, "Stable Elastic Knots With No Self-Contact," J. Mech. Phys. Solids, 116, pp. 33–53.
- [14] Clauvelin, N., Audoly, B., and Neukirch, S., 2009, "Matched Asymptotic Expansions for Twisted Elastic Knots: A Self-Contact Problem With Non-Trivial Contact Topology," J. Mech. Phys. Solids, 57(9), pp. 1623–1656.
- [15] Ibrahim Khalil, M., Tong, D., Wang, G., Khalid Jawed, M., and Khoda, B., 2022, "Systematic Variation of Friction of Rods," ASME J. Appl. Mech., 89(11), p. 111007.
- [16] Sano, T. G., Johanns, P., Grandgeorge, P., Baek, C., and Reis, P. M., 2022, "Exploring the Inner Workings of the Clove Hitch Knot," Extreme Mech. Lett., 55, p. 101788.
- [17] Back, C., Johanns, P., Sano, T. G., Grandgeorge, P., and Reis, P. M., 2021, "Finite Element Modeling of Tight Elastic Knots," ASME J. Appl. Mech., 88(2), p. 024501.
- [18] Kim, S.-H., Yoo, J. C., Wang, J. H., Choi, K. W., Bae, T. S., and Lee, C. Y., 2005, "Arthroscopic Sliding Knot: How Many Additional Half-Hitches Are Really Needed?" Arthrosc. J. Arthrosc. Relat. Surg., 21(4), pp. 405–411.
- [19] Taysi, A. E., Taysi, N. M., and Sismanoglu, S., 2023, "Does Knot Configuration Improve Tensile Characteristics of Monofilament Suture Materials?" J. Oral Maxillo. Surg., 81(1), pp. 72–79.
- [20] Calvaresi, M., Duwez, A.-S., Leigh, D. A., Sluysmans, D., Song, Y., Zerbetto, F., and Zhang, L., 2023, "Mechanical Tightening of a Synthetic Molecular Knot," Chem, 9(1), pp. 65–75.
- [21] Audoly, B., Clauvelin, N., and Neukirch, S., 2007, "Elastic Knots," Phys. Rev. Lett., 99(16), p. 164301.
- [22] Jawed, M. K., Dieleman, P., Audoly, B., and Reis, P. M., 2015, "Untangling the Mechanics and Topology in the Frictional Response of Long Overhand Elastic Knots," Phys. Rev. Lett., 115(11), p. 118302.
- [23] Kang, M. H., Seong, M., Lim, H. W., and Cho, H. Y., 2014, "Simple Method to Restore a Fractured 10-0 Polypropylene Suture Using a Single Fisherman's Knot," J. Catar. Refract. Surg., 40(9), pp. 1568–1570.
- [24] Bergou, M., Wardetzky, M., Robinson, S., Audoly, B., and Grinspun, E., 2008, "Discrete Elastic Rods," ACM Trans. Graph. (TOG), 27(3), p. 63.
- [25] Bergou, M., Audoly, B., Vouga, E., Wardetzky, M., and Grinspun, E., 2010, "Discrete Viscous Threads," ACM Trans. Graph. (TOG), 29(4), p. 116.
- [26] Jawed, M. K., Da, F., Joo, J., Grinspun, E., and Reis, P. M., 2014, "Coiling of Elastic Rods on Rigid Substrates," Proc. Natl. Acad. Sci. U. S. A., 111(41), pp. 14663–14668.
- [27] Tong, D., Borum, A., and Jawed, M. K., 2021, "Automated Stability Testing of Elastic Rods With Helical Centerlines Using a Robotic System," IEEE Rob. Autom. Lett., 7(2), pp. 1126–1133.
- [28] Choi, A., Tong, D., Jawed, M. K., and Joo, J., 2021, "Implicit Contact Model for Discrete Elastic Rods in Knot Tying," ASME J. Appl. Mech., 88(5), p. 051010.
- Discrete Elastic Rods in Knot Tying," ASME J. Appl. Mech., 88(5), p. 051010.
  [29] Tong, D., Choi, A., Joo, J., and Jawed, M. K., 2023, "A Fully Implicit Method for Robust Frictional Contact Handling in Elastic Rods," Extrem. Mech. Lett., 58, p. 101924.
- [30] Lumelsky, V. J., 1985, "On Fast Computation of Distance Between Line Segments," Inf. Process. Lett., 21(2), pp. 55-61.

<sup>2</sup>https://youtu.be/vieLUAQbazo